



JGR Space Physics

RESEARCH ARTICLE

10.1029/2020JA028583

Key Points:

- A model is developed that describes current systems associated with magnetospheric vortices and their dependence on ionospheric parameters
- There is a preferential vortex size that maximizes the current and electron flux
- Based on this model, auroral spot sizes are consistent with Kelvin-Helmholtz structures detected in the boundary layers at Earth and Saturn

Correspondence to:

J. R. Johnson, jrj@andrews.edu

Citation:

Johnson, J. R., Wing, S., Delamere, P., Petrinec, S., & Kavosi, S. (2021). Fieldaligned currents in auroral vortices. *Journal of Geophysical Research: Space Physics*, 126, e2020JA028583. https:// doi.org/10.1029/2020JA028583

Received 13 AUG 2020 Accepted 1 DEC 2020

© 2020. American Geophysical Union. All Rights Reserved.

Field-Aligned Currents in Auroral Vortices

Jay R. Johnson¹, Simon Wing², Peter Delamere³, Steven Petrinec⁴, and Shiva Kavosi⁵

¹Andrews University, Berrien Springs, MI, USA, ²Applied Physics Laboratory, Johns Hopkins University, Laurel, MD, USA, ³Geophysical Institute, University of Alaska, Fairbanks, AK, USA, ⁴Lockheed Martin, Advanced Technology Center, Palo Alto, CA, USA, ⁵University of New Hampshire, Durham, NH, USA

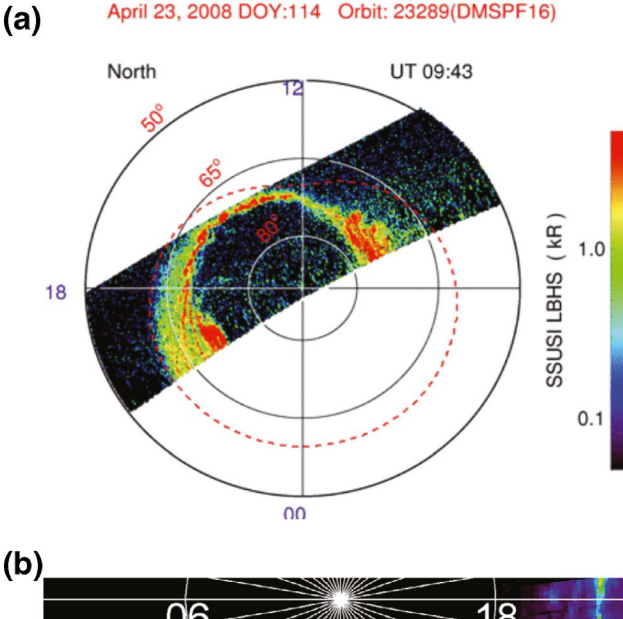
Abstract Auroral bright spots have been observed at Earth, Jupiter, and Saturn in regions that map to the magnetopause boundary layer. It has been suggested that the bright spots are associated with the Kelvin-Helmholtz (KH) instability. We utilize a quasistatic magnetosphere-ionosphere coupling model driven by a vortex in the boundary layer to determine how the field-aligned current structure depends on ionospheric and boundary layer parameters. We compare vortex induced currents with shear-flow induced currents. We find that the strength of the maximum currents are comparable, but the structure is significantly different. For a vortex, the current and electron precipitation maximize when the vortex size mapped to the ionosphere is approximately 1.5L, where $L = \sqrt{\sum_P / \kappa}$ is the auroral scale length, \sum_P is the Pedersen conductivity, and κ is the Knight parameter. For a vortex, the current width provides a direct measure of the size, Δ , of the boundary layer structure, while the current width of shear-flow aurora is generally determined by the larger of Δ or L. For comparison with observations, an event is considered where auroral bright spots in the ionosphere are detected by DMSP SSUSI FUV when KH structures are observed on the dusk flank by THEMIS.

1. Introduction

Velocity shears in the magnetopause boundary layer of Earth and other planets have been correlated with auroral arcs and field-aligned currents (Lundin & Evans, 1985; Sonnerup, 1980). Free energy from the shear is also known to drive Kelvin-Helmholtz instabilities (KHIs) (Johnson et al., 2014) leading to the slow development of Kelvin-Helmholtz (KH) vortex structures (H. Hasegawa et al., 2006, 2009). Some of the most commonly observed auroral features are folds and vortex-like curls (Hallinan & Davis, 1970). Periodic brights spots have been detected by the ultraviolet (UV) imager on the Viking spacecraft (Lui et al., 1989; Potemra et al., 1990). Lui et al. (1989) suggested that the bright spots may be associated with the KHI, which couples to the ionosphere through a field-aligned current system. Figure 1a shows an example of the auroral bead structures detected by the DMSP SSUSI FUV instrument (Paxton et al., 1993) when a KH vortex was simultaneously observed at the magnetopause boundary. Recently, the Cassini spacecraft has detected the presence of bright auroral substructures with a characteristic size ranging from 500 km to thousands of km in the prenoon sector (Grodent et al., 2011) as shown in Figure 1b. The fragmentation of the main ring of emission into small-scale spots appears to be associated with structuring of the field-aligned current system based on magnetic field perturbations observed with Cassini/MAG (Delamere et al., 2013; Talboys et al., 2009a, 2009b; Talboys et al., 2011). Such field-aligned currents naturally develop as KH vortices twist magnetic field lines leading to the suggestion that the vortices result from KHI.

The currents and auroral precipitation associated with KH structures are controlled by the coupling of the magnetopause boundary layer with the ionosphere (Echim et al., 2007, 2008; Lotko et al., 1987; Lyons, 1980; Wei & Lee, 1993). Ionospheric currents are driven by the electric field of the vortex, which maps into the ionosphere. Vortices can drive upward currents in the center of the vortex, and field-aligned potential drops that develop to carry the current can accelerate electrons, which precipitate in the ionosphere. In the case of shear layers, it has been shown that physical properties of the current generator can be inferred from the ionospheric signatures (Echim et al., 2019; Simon Wedlund et al., 2013). In this paper, we examine how the boundary layer and ionospheric parameters control the currents and precipitation, and we examine the differences between vortex driven currents and shear flow driven currents.

JOHNSON ET AL. 1 of 15



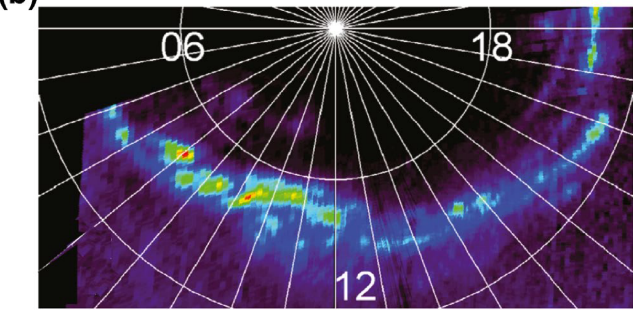


Figure 1. (a) DMSP SSUSI FUV image showing auroral bead structure at 13–18 MLT when Kelvin-Helmholtz vortices were simultaneously observed at the magnetopause boundary on the dusk flank by THEMIS C on April 23, 2008 09:35–09:43 UT. The dashed orange circle is a model auroral equatorward boundary (Zhang & Paxton, 2008). (b) A compilation of three polar views of the northern auroral emission at Saturn obtained with the FUV channel of the Cassini-UVIS spectroimager on August 26, 2008. The image provides a global view of auroral structures obtained over 77 min with a spatial resolution of 200 km (adapted from Figure 1 of Grodent et al. [2011]). A key feature is the cluster of grapes structures, which vary in size and intensity. These structures are thought to be associated with Kelvin-Helmholtz vortices. MLT, magnetic local time.

2. Model

Previously, we examined the dependence of shear-driven field-aligned currents on solar wind and ionospheric parameters (Johnson & Wing, 2015; Wing & Johnson, 2015). We used a one-dimensional model that specified a velocity field intended to model the interface between a flowing boundary layer plasma and a stagnant magnetospheric plasma. In contrast, in the nonlinear stage of KHI, the shear layer is broken up into circulating vortex structures. As in the case of the shear solution, we expect that after a few Alfvén transit times a steady (or slowly evolving) current system would develop as long as the current generator (vortex) remains coherent and moves at a relatively steady speed. Thus, we expect that our description of the current systems would be reasonable as long as the vortex coherence time is longer than the Alfvén transit time. This approximation should be appropriate at Earth for events like those shown in Figure 1a because the timescale of vortex evolution (tens of minutes) is typically longer than the Alfven transit time (minutes). At Jupiter, the Alfvén travel time can be much longer (the order of an hour), but KH structures, such as those shown in Figure 1b, are generally found on the dayside flank region where the sheath flow is opposite the direction of the magnetospheric convection. This region is most unstable because the velocity shear is largest, and the vortices are nearly stationary because the velocity is roughly equal and opposite across the boundary. Therefore even though the Alfvén travel time is long, the vortices themselves can persist in the same location on the order of hours.

The slow development of the vortices allows electrons to respond rapidly along the magnetic field setting up a current voltage relationship, which we characterize by a Knight relationship (Knight, 1973). We then follow the procedure outlined in Johnson and Wing (2015) to obtain a solution for the field-aligned current density for a specified vortex structure.

Following previous studies (De Keyser & Echim, 2013; Echim et al., 2007, 2008; Lyons, 1980; Wei & Lee, 1993), we solve the equation of current continuity in the ionosphere

$$\nabla \cdot \Sigma_P \nabla \phi_i = j_{\parallel} (\phi_m, \phi_i) \tag{1}$$

where ϕ_m and ϕ_i are the potential in the magnetosphere and the ionosphere, respectively, and Σ_P is the height-integrated Pedersen conductivity. The profile of ϕ_m is specified to capture the basic structure of a KH vortex. In our model, the potential drop between the magnetosphere

and the ionosphere drives a parallel current out of the ionosphere determined by a linear Knight relation (Knight, 1973)

$$j_{\parallel} = \kappa(\phi_i - \phi_m),\tag{2}$$

where the Knight conductivity, $\kappa = n_e e^2 / \sqrt{2\pi m_e T_e}$, is controlled by the density and temperature of magnetospheric electrons, which carry the upward field-aligned currents. The linear Knight relation is obtained from an expansion of the nonlinear current-voltage relation when $1 \ll e (\phi_i - \phi_m)/T_e \ll b$ ($b = B_i/B_m$ where B_m and B_i are the magnetic field strength in the magnetosphere and ionosphere, respectively). For simplicity, we will assume that κ is constant throughout the shear layer, recognizing that the current profile will be primarily controlled by the value of density and temperature close to the current maximum.

The assumption of a linear Knight relation is reasonable when the ratio of the potential drop to the average electron thermal energy is smaller than the mirror ratio. This is generally the case at Earth's dayside

JOHNSON ET AL. 2 of 15



Table 1
Comparison of Vortex and Shear Currents

Comparison of vortex and shear Currents			
	Vortex	Shear layer	
$j_{\parallel, ext{max}}$	$\frac{2\Sigma_P V_0 B_0 b}{\Delta_m + 2bL^2 / \Delta_m}$	$\frac{\sum_{P} V_0 B_0 b}{2\left(\Delta_m + \sqrt{b}L\right)}$	
$\Lambda(\Delta_i \ll 2L)$	$2.35\Delta_{\mathrm{i}}$	1.38L	
$\Lambda(\Delta_i \gg 2L)$	$1.67\Delta_{\mathrm{i}}$	$1.76\Delta_{\rm i}$	
$\max_{\Delta}(j_{\parallel,\max})$	$0.57\kappa V_0 B_0 \sqrt{b} L$	$0.5\kappa V_0 B_0 \sqrt{b} L$	
$\Delta_i \left(\max_{\Delta} (j_{\parallel, \max}) \right)$	1.5L	0	
$\Lambda\left(\max_{\Delta}(j_{ ,\max})\right)$	2.8 <i>L</i>	1.38L	

magnetopause as well as the field-aligned current system associated with the breakdown of corotation at Saturn (Johnson & Wing, 2015; Ray et al., 2013). At Jupiter the potential drop associated with the breakdown of corotation can be large and a full Knight relation may be necessary to describe current saturation (Echim et al., 2007; Ray et al., 2009). However, the vorticity associated with KH vortices is typically weaker than that associated with the large-scale boundary flows due to viscous interaction and mixing, and the linear Knight relation can provide some insights. The solutions obtained for the field-aligned current using the linear Knight relation should always be compared with the saturation current, $nev_{the}b / \sqrt{2\pi}$, to ensure their validity.

It should also be noted that the linear Knight relation is most applicable to regions of upward field-aligned current such that currents associated with upcoming ionospheric particles and ambipolar electric fields can be ignored. These conditions are typically found on the dusk flank at earth

where vortex structures typically develop a counterclockwise twist when viewed from above the equatorial plane. As a result, magnetic field lines that are dragged with the structures will develop upward field-aligned currents directed out of both the northern and southern ionospheres. Vortices on the dawn flank generally have the opposite twist and therefore are more likely associated with downward field-aligned currents, which tend to be weaker.

In our previous analysis of the shear layer, we found a simple relationship for the dependence of the current density profile on magnetospheric and ionospheric parameters. The main feature of the profile, maximum current density and thickness, are provided in Table 1. Observations of currents detected in the dayside upward region 1 current system are well organized by the theoretical prediction for the maximum current density (Wing & Johnson, 2015). The currents are driven by potential drop across the shear layer and maximize as the shear increases and width of the boundary layer decreases.

The primary difference between the vortex analysis and previous analysis of shear-driven currents (Echim et al., 2008; Johnson & Wing, 2015; Lyons, 1980) lies in the specification of the magnetospheric potential, $\phi_{\rm m}$. The velocity field is approximated as a cylindrically symmetric vortex, which captures the essential features of the KH structure as illustrated in Figure 2. The main objective here is to model the region near the center of the vortex where the current is concentrated. Previously, we have shown that the width and strength of current profiles determined by our analytic model (Johnson & Wing, 2015) for a shear layer match well with current profiles obtained based on those obtained with a nonlinear Knight relation using a numerical model based on a kinetic equilibrium (Echim et al., 2008).

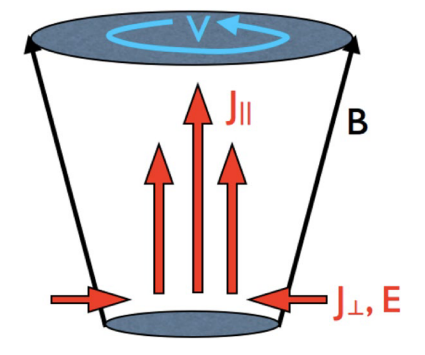


Figure 2. The model includes a driver in the magnetosphere associated with a velocity vortex. The converging electric field of the slowly evolving vortex maps to the ionosphere where it drives Pedersen currents, which are diverted along the magnetic field within the vortex. For simplicity, the vortex is taken to be a cylindrically symmetric velocity ring of characteristic size $\Delta_{\rm m}$ (the radius of the ring at the top).

$$\phi_m(\rho_m) = -V_0 B_0 \Delta_m \exp\left(-\rho_m^2 / 2\Delta_m^2\right)$$
(3)

with a velocity field

$$V_{\varphi}(\rho_m) = \frac{\mathbf{B}_0 \times d\phi(\rho_m) / d\rho_m}{B_0^2} = V_0 \frac{\rho_m}{\Delta_m} \exp(-\rho_m^2 / 2\Delta_m^2)$$
(4)

where ρ_m is a radial coordinate in the magnetosphere and Δ_m is the characteristic scale of the vortex, where the velocity maximizes. This form of the velocity field dictates that we solve Equation 1 in cylindrical coordinates.

Assuming constant conductivity and combining Equations 1 and 2, we find

$$\frac{1}{\rho_i} \frac{d}{d\rho_i} \rho_i \frac{d\phi_i}{d\rho_i} = \frac{\phi_i - \phi_m}{L^2} \tag{5}$$

where $L = \sqrt{\Sigma_P/\kappa}$ is the well-known electrostatic auroral scale length (Lyons, 1980).

JOHNSON ET AL. 3 of 15

In this case, it is useful to employ the azimuthally symmetric

$$\Phi(q) = \int_0^\infty \phi(\rho) J_0(q\rho) \rho d\rho
\phi(\rho) = \int_0^\infty \Phi(q) J_0(q\rho) q dq$$
(6)

where J_0 is a Bessel function of the first kind.

Cylindrical symmetry implies that

$$\Phi_i(q) = \left(\frac{1}{1+q^2L^2}\right)\Phi_m(q) \tag{7}$$

$$\Delta\Phi(q) = \Phi_i - \Phi_m = -\left(\frac{q^2 L^2}{1 + q^2 L^2}\right)\Phi_m \tag{8}$$

$$j_{\parallel}(q) = -\kappa \left(\frac{q^2 L^2}{1 + q^2 L^2}\right) \Phi_m(q) \tag{9}$$

The potential should be expressed in terms of the ionospheric coordinate. Technically, the longitudinal and latitudinal scales would map differently, so a circular structure in the boundary layer would map to an elliptical structure in the ionosphere, but for the purposes of this study, we assume the cylindrical geometry shown in Figure 2 where the coordinate maps symmetrically and flux conservation requires $\rho_m = \sqrt{B_i / B_m} \, \rho_i = \rho_i \sqrt{b}$ and

$$\phi_m(\rho_i) = -V_0 B_0 \Delta_m \exp\left(-\rho_i^2 / 2\Delta_i^2\right) \tag{10}$$

where $\Delta_m = \sqrt{b}\Delta_i$.

Performing the Hankel transform in terms of the radial ionospheric coordinate, ρ_i , we obtain

$$\Phi_{m}(q) = -V_{0}B_{0}\Delta_{m}\int_{0}^{\infty} e^{-\rho^{2}/2\Delta_{i}^{2}} J_{0}(q\rho)\rho d\rho = -V_{0}B_{0}\sqrt{b}\Delta_{i}^{3}e^{-q^{2}\Delta_{i}^{2}/2}$$
(11)

where from now on we let $\rho_i = \rho$. The parallel current density is then obtained by the inverse Hankel transform.

$$j_{\parallel}(\rho) = \sum_{P} V_0 B_0 \sqrt{b} \Delta_i^3 \int_0^\infty \frac{q^2 e^{-q^2 \Delta_i^2 / 2}}{1 + q^2 L^2} J_0(q\rho) q dq$$
 (12)

The maximum value of the current density occurs at the vortex center, $\rho = 0$. Therefore,

$$j_{\parallel,\text{max}} = \lim_{\rho \to 0} \sum_{P} V_0 B_0 \sqrt{b} \Delta_i^3 \int_0^\infty \frac{q^2 e^{-q^2 \Delta_i^2/2}}{1 + q^2 L^2} J_0(q\rho) q dq$$

$$= \frac{\sum_{P} V_0 B_0 \sqrt{b} \Delta_i^3}{2L^4} \int_0^\infty \frac{\mu e^{-2\alpha^2 \mu}}{1 + \mu} d\mu$$

$$= \kappa V_0 B_0 \Delta_m \left[1 - 2\alpha^2 e^{2\alpha^2} E_1(2\alpha^2) \right]$$
(13)

where $\alpha \equiv \Delta_i/2L$ and

$$E_1(z) = \int_1^\infty \frac{e^{-zt}}{t} dt \tag{14}$$

JOHNSON ET AL. 4 of 15

is the exponential integral.

In the limit $\alpha \ll 1$,

$$E_{1}(z) = -\gamma - \log(z) + \sum_{k=1}^{\infty} \frac{(-1)^{k+1} z^{k}}{kk!}$$
(15)

$$j_{\parallel,\text{max}} = \kappa V_0 B_0 \Delta_m \left[1 - 2\alpha^2 \left(1 + 2\alpha^2 + \dots \right) \left(-\gamma - \log \left(2\alpha^2 \right) + 2\alpha^2 + \dots \right) \right]$$

$$= \kappa V_0 B_0 \Delta_m \left(1 + 2\alpha^2 \log \left(2\alpha^2 \right) + \dots \right)$$

$$= \kappa V_0 B_0 \Delta_m \left(1 + \frac{\Delta_i^2}{L^2} \log \left(\Delta_i / L \right) + \dots \right)$$
(16)

It should be noted here that the current is much smaller than for a shear layer by a factor $\mathcal{O}(\alpha)$, cf. Table 1.

For $\alpha \gg 1$

$$E_1(z) \sim \frac{e^{-z}}{z} \left[1 - \frac{1}{z} + \frac{2}{z^2} + \dots \right]$$
 (17)

so that

$$j_{\parallel,\text{max}} \sim \kappa V_0 B_0 \Delta_m \left[1 - \left(1 - \frac{1}{2\alpha^2} + \frac{1}{2\alpha^4} + \dots \right) \right]$$

$$j_{\parallel,\text{max}} \sim \kappa V_0 B_0 \Delta_m \left[\frac{1}{2\alpha^2} - \frac{1}{2\alpha^4} + \dots \right]$$

$$j_{\parallel,\text{max}} \sim 2 \frac{\mathfrak{L}_p V_0 B_0 b}{\Delta_m} \left[1 - \frac{4L^2}{\Delta_i^2} \right]$$
(18)

It should be noted that for large α the maximum current density is enhanced by a factor of 4 relative to the shear layer value.

A uniform approximation (Bender & Orszag, 1978) generally valid for all values of α may be found

$$j_{\parallel,\text{max}} \approx \kappa \frac{V_0 B_0 \Delta_m}{1 + 2\alpha^2} = \frac{2\Sigma_P V_0 B_0 b \Delta_m}{\Delta_m^2 + 2bL^2}$$
(19)

It should be readily apparent that the current density vanishes in either the limit that $\Delta_{\rm m} \rightarrow 0$ or $\Delta_{\rm m} \rightarrow \infty$, and the current density takes on a maximum value at an intermediate value of $\Delta_{\rm m}$. From Equation 13 it can be found that the maximum current density occurs at $\Delta_{\rm i} = 1.5L$ and $j_{\parallel,{\rm max}} = 0.57 \kappa V_0 B_0 L$. This result is in close agreement with that obtained from the uniform approximation (Equation 19) where the maximum current density occurs at $\Delta_i = \sqrt{2}L$ and $j_{\parallel,{\rm max}} = \kappa V_0 B_0 L / \sqrt{2}$.

3. Width of the Vortex Current

Performing a Taylor expansion about the maximum current density at x = 0, we find

$$j_{\parallel}(x) \approx j_{\parallel,\text{max}} \left(1 - \frac{x_i^2}{2\sigma^2} \right) \tag{20}$$

where

$$\sigma = \sqrt{\frac{-j_{\parallel}}{d^2 j_{\parallel} / dx^2}} \bigg|_{x=0}. \tag{21}$$

JOHNSON ET AL. 5 of 15

Taking the second derivative of the current

$$\frac{d^{2}j_{\parallel}}{dx^{2}} = \lim_{\rho \to 0} \Sigma_{P} V_{0} B_{0} \sqrt{b} \Delta_{i}^{3} \int_{0}^{\infty} \frac{q^{2} e^{-q^{2} \Delta_{i}^{2}/2}}{1 + q^{2} L^{2}} \left(\frac{d^{2}}{d\rho^{2}} J_{0}(q\rho) \right) q dq$$

$$= \lim_{\rho \to 0} \Sigma_{P} V_{0} B_{0} \sqrt{b} \Delta_{i}^{3} \int_{0}^{\infty} \frac{q^{2} e^{-q^{2} \Delta_{i}^{2}/2}}{1 + q^{2} L^{2}} \left(\frac{-q^{2}}{2} \left(J_{0}(q\rho) - J_{2}(q\rho) \right) \right) q dq$$

$$= -\frac{\Sigma_{P} V_{0} B_{0} \sqrt{b} \Delta_{i}^{3}}{4 L^{6}} \int_{0}^{\infty} \frac{\mu^{2} e^{-2\alpha^{2} \mu}}{1 + \mu} d\mu$$

$$= -\kappa \frac{V_{0} B_{0} \Delta_{m}}{2 L^{2}} \left[\frac{1}{2\alpha^{2}} - \left(1 - 2\alpha^{2} e^{2\alpha^{2}} E_{1}(2\alpha^{2}) \right) \right]$$
(22)

Then for $\alpha \ll 1$

$$\sigma \approx \Delta_i$$
 (23)

while for $\alpha \gg 1$

$$\sigma \approx \frac{\Delta_i}{2} \tag{24}$$

In contrast with the shear layer, the width of the current layer mostly depends on the size of the driver. An estimate for the full width at half maximum (Λ) can be obtained by recognizing that if the current density were fit to a Gaussian of width σ , $\Lambda = 2\sqrt{2 \ln 2}\sigma$.

4. The Spatial Dependence of the Current

Having established the typical strength and width of the current structure associated with a vortex, it is useful to examine the exact solution of Equation 12 obtained from direct integration using standard methods. The results are presented in Figure 3. The parallel current density is shown as a function of x/L (same as ρ_i/L) in panel (a). In panel (b) the normalized current, $j_{\parallel}/j_{\parallel,\text{max}}$ is shown. For comparison, panels (c) and (d) show the same variables for a shear layer having a velocity changing from $V = V_0$ to V = 0 over a distance of Δ_m (Johnson & Wing, 2015).

$$j_{\parallel}^{s}(x) = \kappa \frac{V_{0}B_{0}\Delta_{m}}{2} \left[\frac{\pi}{2} \frac{e^{-|x|/L}}{\sin(\pi\alpha)} + \sum_{n=1}^{\infty} (-1)^{n} \frac{ne^{-2n|x|/\Delta_{i}}}{n^{2} - \alpha^{2}} \right]$$
(25)

The width of the current layer is obtained directly from panels (b) and (d) as the isocontour where $j_{\parallel}(\Lambda/2) = j_{\parallel,\rm max}/2$. For the vortex, the analytic width for small and large α (Equations 23 and 24) are shown as broken yellow and magenta lines. It is apparent from the isocontour that the width vanishes as $\alpha \to 0$ in panel (b), whereas it reaches a limiting value on the order of L in panel (c). It should also be noted that a small return current density (not shown) is found at larger radial distance. We do not emphasize the downward return current primarily because we are focusing on the central current in the vortex and the width of the upward current channel. Our model for the current voltage relationship is most appropriate for the upward current region, and may be inaccurate in the downward current region where the role of ionospheric electrons is important. However, in numerical models that do include a more complete description of both the upward and downward current regions, we have found that the current profile of the upward current region (Echim et al., 2007) is generally well described by our analytic solutions (Johnson & Wing, 2015).

To gain further insight regarding mapping between the magnetosphere and ionosphere, we show in Figure 4 the mapped magnetospheric potential, $\phi_{\rm m}$ ($\rho_{\rm i}$), and the numerical solution for the ionospheric potential,

JOHNSON ET AL. 6 of 15

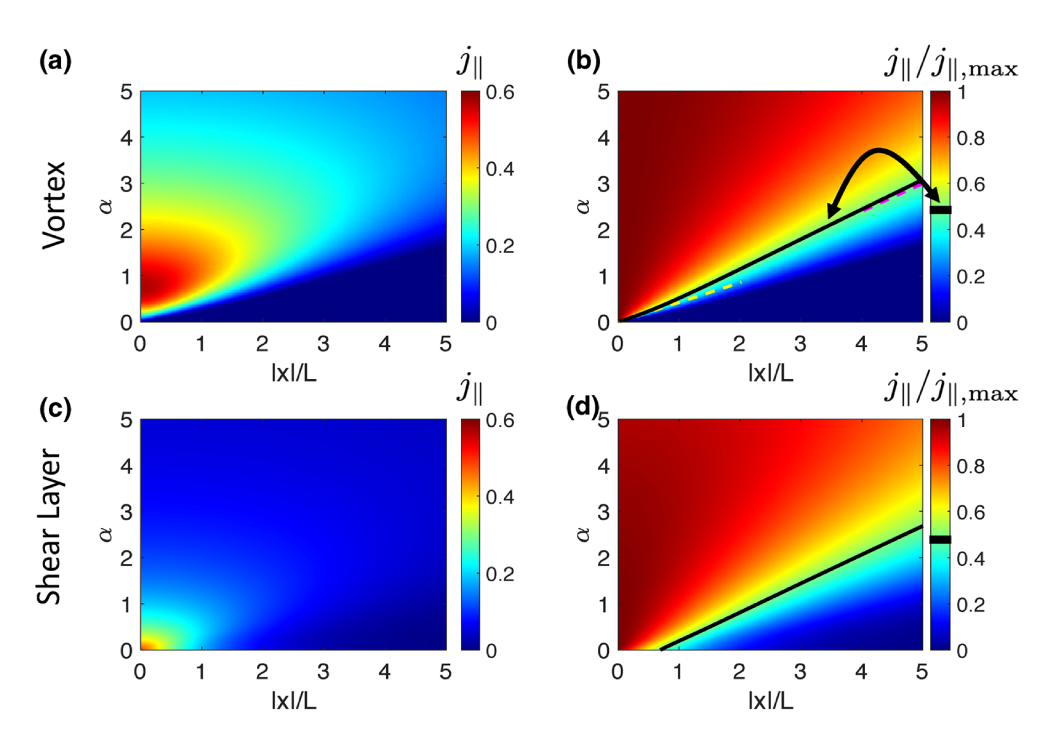


Figure 3. The spatial profile of the current density as a function of x/L for different values of $\alpha = \Delta_i/2L$. Panels (a) and (b) show the current density and normalized current density for the vortex solution. Panels (c) and (d) show current density and normalized current density for the shear-layer solution. The black line in panels (b) and (d) show the half width of the current density for the vortex solution. The yellow and magenta dashed lines show the width based on Equations 23 and 24.

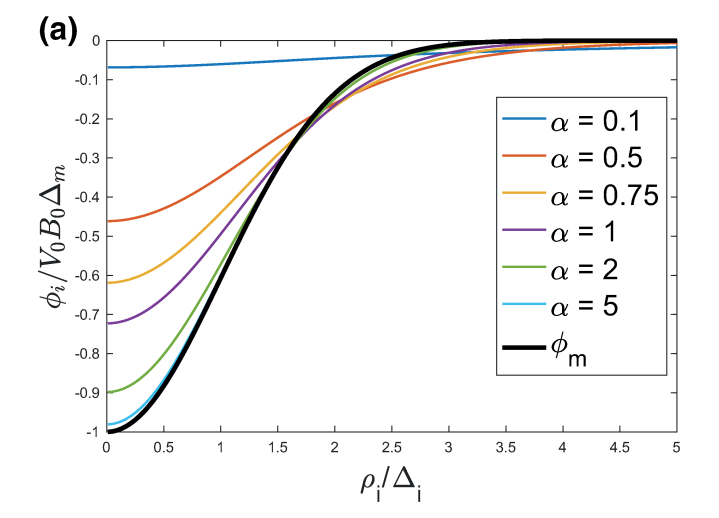
$$\phi_i(\rho_i) = -V_0 B_0 \Delta_m \left[4\alpha^2 \int_0^\infty \frac{y e^{-y^2/2}}{y^2 + 4\alpha^2} J_0\left(\frac{\rho_i}{\Delta_i} y\right) dy \right]$$
(26)

as well as the parallel current. From Figure 4a, it is apparent that the half-width of the potential is only weakly dependent on α and is essentially the same as the half-width of the mapped magnetospheric potential. However, the strength of the potential is substantially reduced when the vortex size mapped to the ionosphere is less than L ($\alpha \lesssim 1$). This result is similar to the shear layer solution where the ionospheric potential does not map on scales smaller than L.

In Figure 4b, we show the current associated with this potential drop (scaled to $\kappa V_0 B_0 \sqrt{b} \Delta_m$). For a shear layer, it is well known that width of the current channel will broaden to the electrostatic scale, L, even when mapped gradient scale length of the driver is less than L (Johnson & Wing, 2015; Lyons, 1980). In contrast to the shear layer, when the vortex size is smaller than L, the current channel does not broaden significantly beyond the mapped vortex size Δ_i . It is also apparent from the plot of the potential in Figure 4a that $\phi_i - \phi_m$ changes sign and therefore the parallel current also changes sign consistent with a small downward current density at larger radial distance as mentioned above. Although the normalized current in this plot appears to be monotonically decreasing as α increases, it should be noted that the actual current density is multiplied by a factor of Δ_m , which ultimately leads to the maximum current density at $\alpha=0.75$ shown in Figure 3. These results demonstrate that the size of the auroral vortex structure maps directly to a boundary layer structure of the same size. In contrast, auroral structures driven by a velocity shear may be much broader than the size of the driver if $\Delta_i \lesssim L$.

The physical picture of the current system is that of an ionospheric current that converges on the center of the vortex where it is diverted upwards along the magnetic field. The converging ionospheric current is driven by the vortex electric field associated with the mapped potential. At first glance, one might expect that as the size of the vortex decreases that the current would intensify in the center of the vortex, but

JOHNSON ET AL. 7 of 15



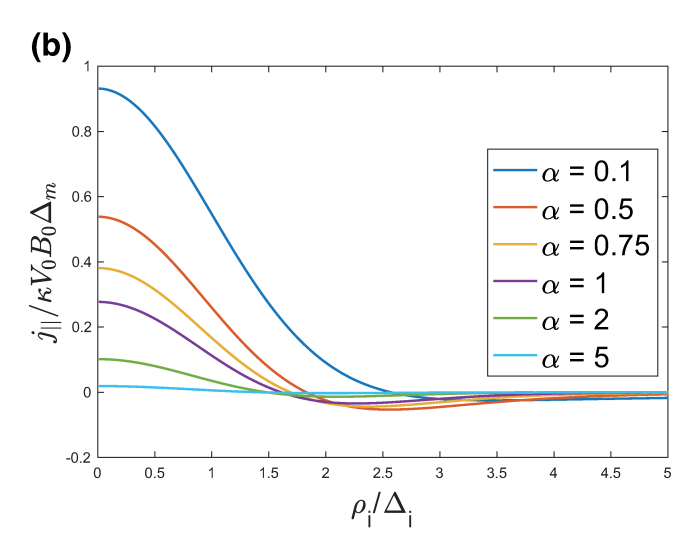


Figure 4. (a) The ionospheric potential and magnetospheric potential are shown as a function of ρ_i/Δ_i for different values of $\alpha=\Delta_i/2L$. The potential maps well to the ionosphere for $\alpha\gg 1$, while the strength of the ionospheric potential is substantially reduced for $\alpha\lesssim 1$. In all cases, the width of the ionospheric potential scales with Δ_i . (b) The spatial profile of the current density as a function of ρ_i/Δ_i for different values of α . The width of the current layer scales with Δ_i with a reduction by a factor of 2 at larger values of α as shown in Section 3.

our solutions show that the current is choked out. To understand this result, we need to consider differences in how the electric field maps between the shear layer solution and vortex solution. The strength of the electric field in the magnetosphere for both the shear layer and vortex is approximately V_0B_0 and, if the potential maps to the ionosphere, will correspond to an ionospheric electric field $V_0B_0\sqrt{b}$. In the case of the shear layer, this electric field drives a current per unit length $\Sigma_P V_0 B_0 \sqrt{b}$ into the shear layer. In the limit that the shear layer width is much smaller than L, the upward current flow channel broadens to a thickness of L so that if we consider current continuity

$$j_{\parallel} \sim \frac{\Sigma_P V_0 B_0 \sqrt{b}}{L} \tag{27}$$

as shown in Johnson and Wing (2015).

For a vortex, the ionospheric current is converging radially inward and therefore the total current flowing into the center of the vortex is

$$I_{\perp} = \Sigma_P E_{\perp} 2\pi \Delta_i, \tag{28}$$

where E_{\perp} is the radial electric field. As we have shown, the upward current is confined to the center of the vortex so $I_{\parallel} \sim j_{\parallel}\pi\Delta_i^2$. Thus, from current continuity, we have

$$j_{\parallel} \sim \frac{2\Sigma_P E_{\perp}}{\Delta_i} \tag{29}$$

This result suggests that as Δ_i decreases, that the current increases due to the convergent geometry, and is consistent with Equation 18 in the limit that $\alpha\gg 1$ where the magnetospheric potential maps to the ionosphere with an electric field $E_\perp=V_0B_0\sqrt{b}$. However, when the size of the vortex is less than L the electric field decreases because the magnitude of the potential does not map on that scale. To see this effect, we can compute the electric field for $\alpha\ll 1$ directly from Equation 26

$$E_{\perp}(\rho_{i}) = -\frac{1}{\Delta_{i}} \frac{d\phi_{i}(\rho_{i})}{d\rho_{i}} = -V_{0}B_{0}\sqrt{b} \left[4\alpha^{2} \int_{0}^{\infty} \frac{y^{2}}{y^{2} + 4\alpha^{2}} e^{-y^{2}/2} J_{1}\left(\frac{\rho_{i}}{\Delta_{i}}y\right) dy \right]$$

$$\approx -V_{0}B_{0}\sqrt{b} \frac{\Delta_{i}^{2}}{L^{2}} \left(\frac{1 - e^{-\rho_{i}^{2}/2\Delta_{i}^{2}}}{\rho_{i}/\Delta_{i}} \right)$$
(30)

The maximum electric field $E_{\perp, \rm max} = -0.45 V_0 B_0 \sqrt{b} \Delta_i^2 / L^2$ occurs at $\rho_i = 1.59 \Delta_i$. As such, it can be seen that for $\alpha \ll 1$

$$j_{\parallel} \sim \frac{\sum_{P} V_0 B_0 \sqrt{b} \Delta_i}{I^2} \tag{31}$$

consistent with the solution that was obtained in Equation 16. We can therefore conclude that two important physical effects lead to the current maximum found at $\alpha = 0.75$. The convergent geometry leads to an increased current density as the size of the vortex decreases; however, when the vortex size becomes smaller than the electrostatic auroral scale, L, the electric field no longer penetrates into the ionosphere and the current is choked out. The maximum current occurs at a scale where the convergence is as large as it can be without choking out the current.

It is also interesting to compare the total current in the vortex and shear layer solutions. For the shear layer, the current density in Equation 25 can be integrated across the shear layer, and the summation can be performed leading to a current per unit length

JOHNSON ET AL. 8 of 15

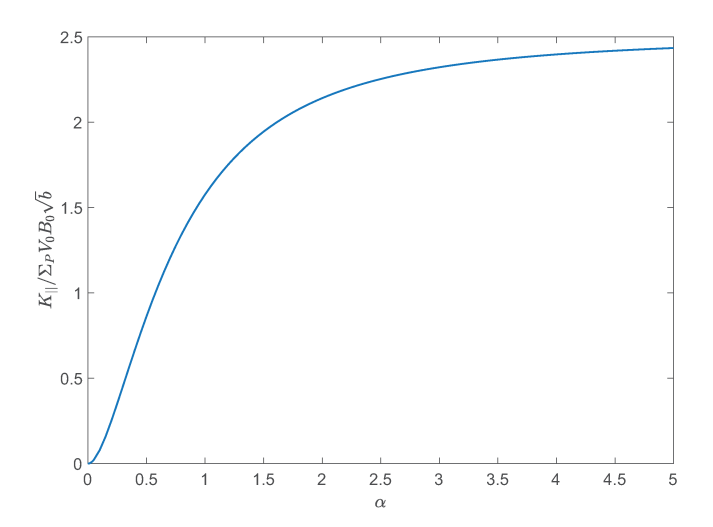


Figure 5. Current per unit length, $K_{\parallel}^{\parallel}$, obtained by integrating the current density along a trajectory that passes through the center of the vortex compared with the parallel current per unit length, K_{\parallel}^{s} , integrated along a trajectory that passes through an equivalent shear layer. Note that the surface current is roughly the same for the vortex and shear layer at the optimum scale $\alpha = 0.75$.

$$K_{||}^{s} = \int_{-\infty}^{\infty} j_{||}^{s}(x) dx = \sum_{P} V_{0} B_{0} \sqrt{b}$$
 (32)

that is independent of the current width, Δ_m . This current per unit length can be compared with that of a slice through the center of the vortex,

$$K_{\parallel}^{\nu} = 2 \int_{0}^{\infty} j_{\parallel}(\rho) d\rho = 2 \Sigma_{P} V_{0} B_{0} \sqrt{b} \Delta_{i}^{3} \int_{0}^{\infty} \int_{0}^{\infty} \frac{q^{2} e^{-q^{2} \Delta_{i}^{2} / 2}}{1 + q^{2} L^{2}} J_{0}(q\rho) q dq d\rho \quad (33)$$

which can be simplified using $\int_0^\infty q J_0(q\rho) d\rho = 1$.

$$\frac{K_{\parallel}^{v}}{K_{\parallel}^{s}} = 8\alpha^{2} \int_{0}^{\infty} \frac{y^{2} e^{-y^{2}/2}}{y^{2} + 4\alpha^{2}} dy = 8\alpha^{2} \left(\frac{\sqrt{2\pi}}{2} - \pi\alpha e^{-2\alpha^{2}} \operatorname{erfc}\left(\sqrt{2}\alpha\right) \right)$$
(34)

We show K_{\parallel}^{v} of the vortex as a function of the size of the vortex in Figure 5. For a small vortex size, $\alpha \ll 1$, K_{\parallel}^{v} is much smaller K_{\parallel}^{s} of the shear layer mainly because the current is choked out as described above. For a larger vortex size, the curvature becomes smaller and the slice through the vortex looks like a slice across a shear layer having velocity that changes from $V = V_0$ on one side to $V = -V_0$ on the other side. As such, the current per unit length is about twice as large as the shear layer (for which the velocity changes from $V = V_0$ to V = 0).

5. Auroral Vortex Observations

5.1. Auroral Vortex at Earth

For the April 23, 2008 09:35–09:43 UT event shown in Figure 1a, we have simultaneous observations of DMSP F16 SSUSI FUV imager (Paxton et al., 1993), SSJ5 particle precipitation (Hardy et al., 1984), magnetic field (Rich et al., 1985), THEMIS B and C magnetic field (Auster et al., 2008) and plasma (McFadden et al., 2008). This event has been identified as a KH event in the survey performed by Kavosi and Raeder (2015). This event is further independently checked with the Hasegawa (1975) KHI criterion under the assumption of plasma incompressibility and no boundary thickness,

$$\left[\mathbf{k}\cdot\left(\mathbf{V}_{1}-\mathbf{V}_{2}\right)\right]^{2} > \frac{\rho_{1}+\rho_{2}}{\mu_{0}\rho_{1}\rho_{2}}\left[\mathbf{k}\cdot\left(\mathbf{B}_{1}+\mathbf{B}_{2}\right)\right]^{2}$$
(35)

where subscripts 1 and 2 refer to either side of the magnetopause, ρ , V, B, μ_0 , and \mathbf{k} are mass density, flow velocity, magnetic field, magnetic permeability constant, and the wave vector \mathbf{k} , respectively. THEMIS C, which was located at the magnetopause boundary layer, provides the plasma and magnetic field observations in the magnetosheath and magnetosphere. Assuming that the wave propagates primarily along the magnetopause (LM plane), the ratio of the left-hand over the right-hand side of Equation 35 is 3.1, satisfying the KHI threshold. The average solar wind conditions for this event are: solar wind speed V = 567 km/s, n = 4.7 cm⁻³, dynamic pressure = 2.9 nPa, and IMF(B_x , B_y , B_z) = (3.5, -7.1, -5.3) nT. These solar wind parameters are obtained by matching the IMF clock angle between ACE and THEMIS B, which was located in the magnetosheath proper, not too far from THEMIS C. This procedure produces a time lag of 46 min between ACE and THEMIS B. THEMIS B and C were located at GSM(x, y, z) = (-0.9, 25.9, -4.3) R_E and GSM(x, y, z) = (-5.4, 18.6, -2.2) R_E , respectively. The solar wind data from NASA OMNIweb show similar values. The magnetic field directions have clock angles ~220°-300°, which are probably not the most favorable IMF clock angles for the KH instability, but 14%-28% of KHIs at the Earth's magnetopause occur under these IMF conditions (Kavosi & Raeder, 2015).

JOHNSON ET AL. 9 of 15

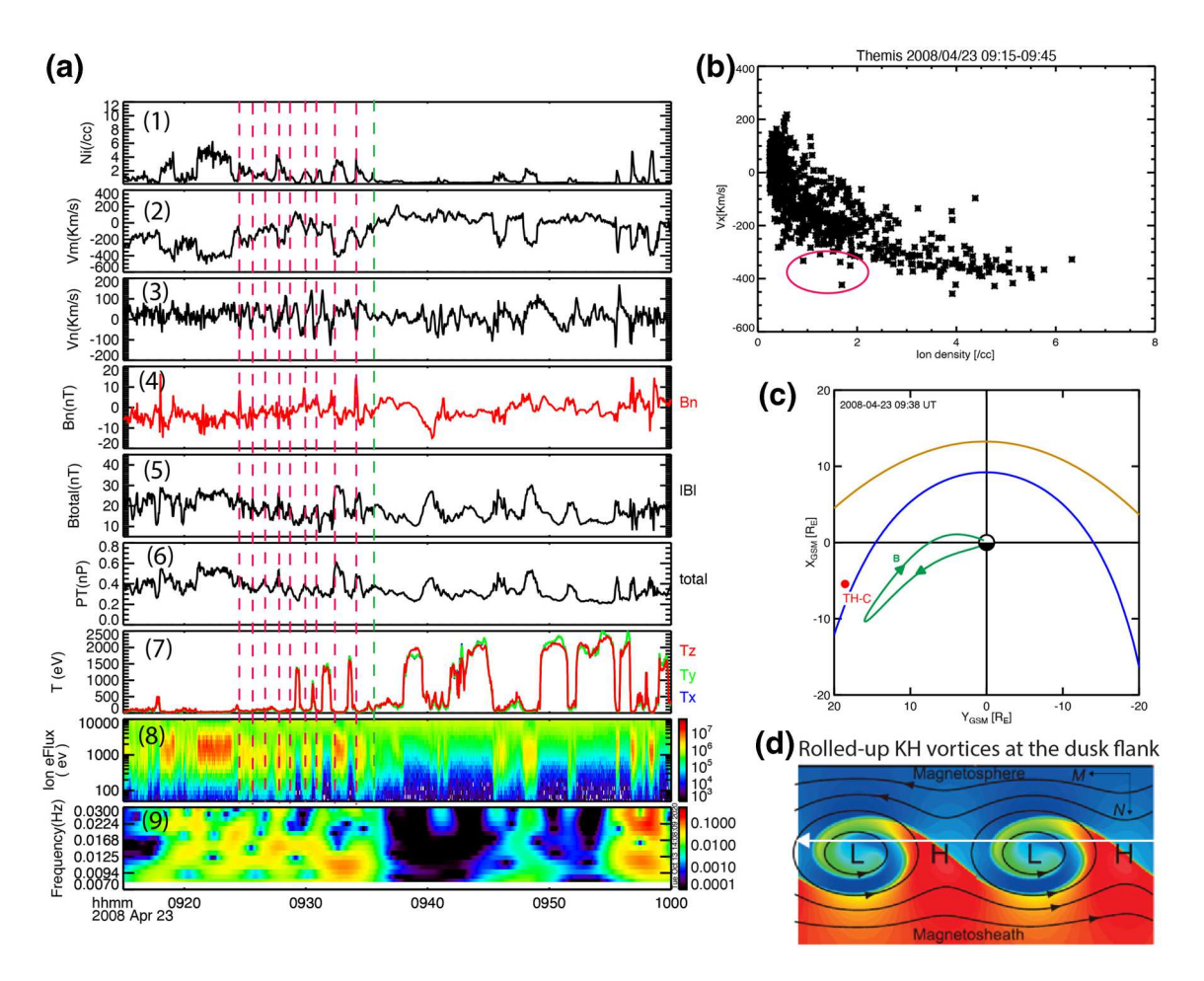


Figure 6. THEMIS C observations for the April 23, 2008 event shown in Figure 1a. (a) From top to bottom, the ion number density, ion $V_{\rm M}$, ion $V_{\rm N}$, $B_{\rm N}$, $B_{\rm N}$, $B_{\rm N}$, total (plasma + magnetic) pressure, $T_{\rm e}$, and wavelet spectra of the total pressure. To help visualize the pressure, temperature, density, and velocity semi-periodic fluctuations, red and green vertical dashed lines marking the maxima in total pressure are drawn. The green vertical dashed line is adjacent to the vortex, the properties of which are calculated in Section 5.1. (b) Ion V_x versus n_i plot showing pattern that is more similar to that for small vortex size in H. Hasegawa et al. (2006).(c) The T96 magnetic field line tracing (green curve) from the DMSP F16 to the magnetosphere projected to the equatorial plane. The THEMIS C location, which is only slightly (2.2 $R_{\rm E}$) below the equatorial plane, is within several $R_{\rm E}$ from the magnetic field line trace. The blue and gold curves indicate the magnetopause (Shue et al., 1998) and bow shock locations (Chao et al., 2002). (d) Schematic drawing of rolled-up KH vortices at the dusk-flank magnetopause showing the relationship between the streamline pattern (black lines) and total (magnetic plus plasma) pressure and density (red, dense; blue, tenuous) distributions, when viewed in the vortex rest frame (from H. Hasegawa [2012]). The subsolar region is to the left. The total pressure minimizes at the center (L) of the vortices, while it maximizes at the hyperbolic point (H), which is a flow stagnation point in the vortex rest frame, and around which the streamlines form hyperbolas (Miura, 1997). It is expected that magnetosphere-to-magnetosheath transitions be characterized by large and rapid density increases that approximately coincide with maxima in the total pressure (panel a).

Figure 6a shows quasiperiodic fluctuations of the bulk plasma and magnetic field parameters during the interval 0915–0940 UT. The figure shows the THEMIS C magnetic field and velocity components in boundary normal coordinates (L, M, N) to facilitate the characterization of the oscillations. Oscillations occur, where the THEMIS C observes alternately hot magnetosphere plasma and cold magnetosheath plasma (panel a_8). The oscillations are also visible in the magnetic field normal component, BN (panel a_4), the M and N components of the smoothed velocity (panel $a_{(2,3)}$), the ion number density (panel a_1) and the total pressure (magnetic plus ion pressure; panel a_6). The vertical red dashed lines indicate where the total (plasma + magnetic) pressure maximize. As depicted in Figure 6d, within a rolled-up vortex the total pressure is expected to have a minimum (indicated by L) at the center and a maximum at the edge of the vortex (indicated by H). The pressure minimum occurs because the centrifugal force of the rotating vortex pushes the plasma radially outward. Therefore, the total pressure is expected to maximize at the edge of the vortex as indicated by the red vertical dashed line. Panel a_9 shows the wavelet spectra of the total pressure. The average KH wave period for this event can be estimated at \sim 70 s.

JOHNSON ET AL. 10 of 15



From Figure 6a and from the plot of the same parameters from a larger time scale, 08:00 to 10:00 UT (not shown), it can be estimated that the electron magnetospheric temperature \sim 1 keV and density \sim 0.3 cm⁻³ and magnetosheath temperature \sim 20 eV and density \sim 10 cm⁻³. The plasma in the KH vortex is a mixture of that of magnetosphere and magnetosheath and the electron temperature and density would fall somewhere in between those of the magnetosphere and magnetosheath. THEMIS C appears to be located inside a KH vortex and perhaps near its center around 09:35 UT, slightly to the right of the green vertical dashed line in Figure 6a, when it observes $T_{\rm e} \sim 300$ eV, $n_{\rm e} \sim 1$ cm⁻³, and a small tailward velocity of $V_x > -50$ km/s (not shown) with $V_{\rm N}$ is nearly 0. The Knight relation conductivity κ can then be calculated (see Equation 2) from these values of $T_{\rm e}$ and $n_{\rm e}$.

The DMSP F16 observes a small scale upward field-aligned current and a band of monoenergetic electron precipitation near dusk at ~17:10 magnetic local time (MLT) and magnetic latitude (MLat) ~70°-71° near the open-closed boundary of the auroral oval where the solar zenith angle $\chi \sim 76^\circ$. At this solar zenith angle and with the observed 10.7 cm solar flux density = 71.1 × 10^{-22} W/(m²·Hz), one can obtain the Pedersen conductivity due to the ionizing solar extreme (UV) radiation is $\Sigma_{\rm p,s} \sim 3.6 \rm S$ from the Robinson and Vondrak (1984) formula (a similar value can be obtained from Ieda et al. [2014]). The DMSP SSJ5 observes the average peak electron energy $E_{\rm e} = 480$ eV, and electron energy flux $\varepsilon = 1.8$ ergs/(cm²·s), from which one can obtain the Pedersen conductivity due to electron precipitation $\Sigma_{\rm p,e} = 1.6 \rm S$ using the Robinson et al. (1987) formula. The total $\Sigma_p = \sqrt{\Sigma_{p,s}^2 + \Sigma_{p,e}^2} \sim 3.9 \, \rm S$ (Wallis & Budzinski, 1981). Using these calculated values of Σ_p and κ , one can obtain an auroral electrostatic scale length = $\sqrt{\Sigma_p/\kappa} = 50 \rm km$. From the DMSP magnetic field data or from the size of the auroral bead in the SSUSI image in Figure 1a, one can obtain the current width $\Lambda = 126 \, \rm km$, which would give $\Lambda / L = 2.5$. Table 1 shows that the optimal condition for the maximum current width occurs when $\Lambda / L = 2.8$, which is very close to the observed value of 2.5.

The spatial scale of the KH vortex at the magnetopause boundary can be estimated from the observed value of Λ /L = 2.5. From the definition of Λ as the FWHM, the current should drop by a factor of 2 at $|x| = \Lambda$ /2 or |x|/L = 1.3. In Figure 3b, the black curve defines the half-max for a given α and it can be seen that |x|/L = 1.3 corresponds to $\alpha \approx 0.7$. The radius of the KH vortex scale mapped to the ionosphere is therefore $\Delta_i = 2\alpha L = 70$ km. The radius of the KH vortex at the magnetopause boundary $\Delta_m = \sqrt{b}\Delta_i = 3.2 \times 10^3 \text{km} \sim 0.5 \text{R}_E$, where $b = B_i/B_m$, B_m is the magnetic field magnitude at the magnetopause and B_i is the magnetic field magnitude at the ionosphere. Here, we have estimated the values of $B_m = 20$ nT and $B_i = 4.1 \times 10^4$ nT from the magnetic field observations from THEMIS C (vertical dashed green curve in panel a_5 in Figure 6a) and DMSP (not shown), respectively.

The spatial scale of the KH vortex obtained from the theory can be compared with that estimated from the THEMIS C in situ observations at the magnetopause boundary layer. The tailward speed of the KH vortex structure (the phase velocity) can be estimated as the vortex center-of-mass velocity $V_{\rm vc} = \sum (\rho V)/\sum \rho$ (Lin et al., 2014). Lin et al. (2014) compared this method with the four-spacecraft-timing-analysis method, which is deemed to be more accurate, found that the velocities obtained from the center-of-mass velocity method are within 20% of those obtained from four-spacecraft-timing-analysis method. Using the center-of-mass method, the phase velocity of the vortex is estimated to be $V_{\rm vc} \sim 200$ km/s. Using this estimate for $V_{\rm vc}$ and the periodicity of ~70 s, the KH wavelength can be estimated to be ~14,000 km/s or ~2.2 $R_{\rm E}$. Otto and Fairfield (2000) and Fairfield et al. (2000) found that the KH vortex size is about one-half the wavelength. Assuming the same scaling relationship, the KH vortex size can be estimated to be ~1.1 $R_{\rm E}$, which is very close to ~1 $R_{\rm E}$ for the diameter (or radius ~0.5 $R_{\rm E}$) of the KH vortex obtained from the theory, ionospheric observations (precipitating electron average energy, energy flux, |B|, Λ), and boundary layer observations ($T_{\rm e}$, $T_{\rm e}$, $T_{\rm e}$).

The observed KH wavelength of $\sim 2.2R_{\rm E}$ is smaller than the previously reported wavelength of $3-4R_{\rm E}$ reported by Hasegawa et al. (2006). It also falls in the low end of the range of KH wavelengths of $2-14R_{\rm E}$ in the 14 events reported by Lin et al. (2014). Likewise, the vortex size of 1 or $1.1R_{\rm E}$ is smaller than the previously reported value of $2R_{\rm E}$ by Fairfield et al. (2000).

Figure 6b plots the V_x versus n_i , which has been previously used to test for the presence of a KH vortex (Hasegawa et al., 2006). In a rolled-up KH vortex, the magnetospheric plasma that extends into the magnetosheath and forms part of the breaking wave gets accelerated to speeds larger than the magnetospher-

JOHNSON ET AL. 11 of 15

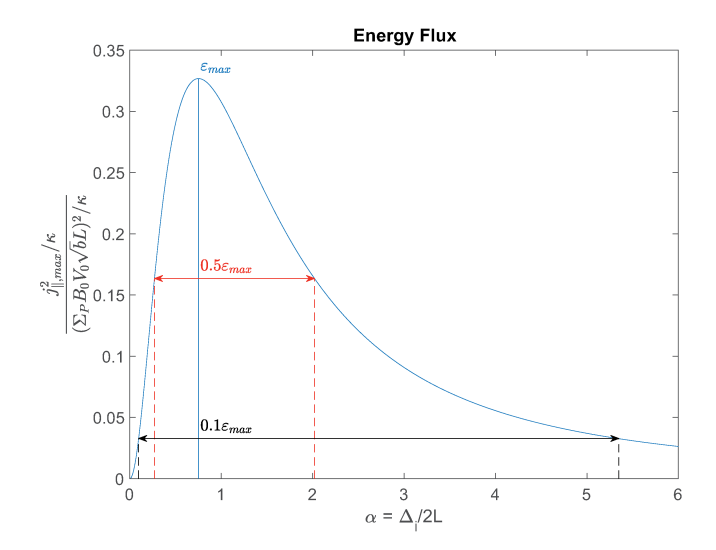


Figure 7. Maximum energy flux (j_\parallel^2/κ) versus scale of the vortex $(\alpha=\Delta_i/2L)$, mapped to the ionosphere based on Equation 13. The energy flux peaks at $\alpha=0.75$. The flux drops by a factor of 2 outside the range $0.27<\alpha<2$, and the energy flux drops by a factor of 10 outside the range $0.1<\alpha<5.35$. From the DMSP observations shown in Figure 1a, we can infer that $\alpha\approx0.7$, which is very close to the optimum size that maximizes the current and energy flux.

ic speed. This effect can be seen in a V_x versus n_i scatter plot where the KH wave or vortex exhibits a distinct pattern depending on the phase of the KHI growth. Figure 6b shows that this event is evolved but not yet completely rolled up because a small fraction of the low-density magnetospheric plasmas $< 2 \text{ cm}^{-3}$ flows faster than the magnetosheath plasma > 350 km/s (within the red dashed circle in Figure 6b). Moreover, Hasegawa et al. (2006) presents V_x versus n_i plots of simulation data for three categories: (1) well developed rolled up big vortex, (2) weakly rolled up small or moderate size vortex (3) no vortex. The V_x versus n_i plot in Figure 6b is more similar qualitatively to that for the small vortex than for the large vortex in Hasegawa et al. (2006), which would be consistent with the rather small or moderate vortex size estimated using either method presented above.

The KH vortex size of $1R_{\rm E}$ and $\Lambda/L=2.5$ are computed from electron precipitation and magnetic field observed by DMSP F16 and $T_{\rm e}$, $n_{\rm e}$, and B observed by THEMIS C. Figure 6c traces the magnetic field from the DMSP F16 location at MLT ~17:10 and MLat ~71° when it observes the auroral bead, small scale upward FAC, and monoenergetic electrons to the magnetosphere using Tsyganenko magnetic field model (T96; Tsyganenko & Stern, 1996). The figure shows that the magnetic field line from the DMSP F16 location does not trace exactly to THEMIS C, although the trace comes to within several $R_{\rm E}$ of THEMIS C. It seems to suggest that the T96 field line mapping is not entirely accurate for this particular event because had it been perfect, the location of the DMSP F16 at the openclosed boundary of the oval would map to the magnetopause boundary.

Irrespective of the accuracy of T96, for the rough calculation presented here (with one or two significant figures), it may not be necessary for the two spacecraft to be located exactly on the same field line. MHD simulations show that typically the KH vortex does not occur in isolation, but rather there is a train of KH vortices that move from near noon to the nightside along the flank of the magnetopause boundary (Merkin et al., 2013). This feature discriminates KH waves from flux-transfer events, and other surface waves at the magnetopause. This picture is consistent with the multiple auroral beads seen in Figure 1a and the semi-periodic fluctuations seen in the temperature, density, and velocity plots in Figure 6a. The DMSP observations at 17:10 MLT would be expected to map to a magnetopause location past the terminator on the nightside and THEMIS C is located on the nightside at $GSM(x, y, z) = (-5.4, 18.6, -2.2)R_E$. The magnetosheath plasma and magnetic field properties evolve rapidly from noon to dusk, but typically evolve more slowly on the nightside as they asymptotically approach the solar wind values (Spreiter & Stahara, 1985). Thus, the T_e , n_e , and T_e 0 observed by THEMIS C may not map exactly to the DMSP F16, but these plasma and magnetic field line properties are likely to be similar to those at the KH vortex that does map to the DMSP F16 location.

The size of the vortex is generally controlled by processes in the region of instability. However, ionospheric signatures of a vortex (field-aligned current and electron precipitation) will be most easily detected when the size of the vortex is within a certain range. It is likely that as vortices develop nonlinearly as they move from the dayside to the flank, their size would evolve through a range of scales; however, the vortices would be most visible in the ionosphere when their size is optimal. Note that not all DMSP SSUSI observations for KH events show clear bead structures such as the ones shown in Figure 1a, which may be attributed to nonoptimal conditions for obtaining maximum current width and mapping the vortices from the magnetopause boundary to the ionosphere.

Figure 7 suggests that electron flux (scaling as $j_{\parallel}\Delta\phi=j_{\parallel}^2/\kappa$) is reduced by a factor of 2 outside of the range 0.27 < α < 2, which for the conditions of this event correspond to a range of $\Delta_{\rm m}$ (vortex radius) from 0.2 to 1.4 $R_{\rm E}$. Structures outside this range would not be distinguishable from the ambient UV emissions in Figure 1a. The conditions favorable to auroral bead structures associated with KH events will be investigated in our follow-up observational study.

JOHNSON ET AL. 12 of 15



5.2. Auroral Vortex at Saturn

At Saturn, the fragmentation of the main ring of emission into small-scale spots shown in (Figure 1b) is suggestive of a similar process. Typical auroral features are localized (500-2,000 km) auroral bright spots (10-30 kR) that map to the boundary layer. As shown in Figure 7 it is expected that the peak energy flux occurs for scales satisfying $\alpha = 0.75$ and in this regime, the width of the energy flux is $\Lambda_{\epsilon} \approx 1.6\Delta_{i}$. The most prominent scale associated with the bright spots is $\Lambda_{\varepsilon} \approx 2,000$ km, which maps to $\Delta_{\rm m} \approx 1R_{\rm S}$ in the boundary layer (using $\sqrt{B_i}/B_m \sim 60$, and is consistent with the size of KH structures (Grodent et al., 2011; Masters et al., 2010, 2011). Using the theory mentioned above, it should be possible to compare the expected auroral intensity versus scale (Δ) to see if the distribution follows the expected trend, and to constrain L (ionospheric conductivity) based on the peak intensity.

6. Discussion and Conclusions

The field-aligned current properties of a shear layer are compared with that of a vortex in Table 1. In the limit that $\Delta_i \gg L$ the maximum current density has essentially the same behavior for shear layers and vortices and the current width scales with Δ_i . The primary difference is in the limit $\Delta_i \ll L$. In this case, the shear layer becomes a discontinuity, but the current in the shear layer spreads out to the auroral scale, L and the current maximizes at $j_{\parallel,\text{max}} = 0.5 \kappa V_0 B_0 L \sqrt{b}$. On the other hand, the vortex current does not broaden and the current is confined in the vortex structure. As the width of the vortex vanishes, $\Delta \rightarrow 0$, the current scales with $j_{\parallel, max} = \kappa V_0 B_0 \Delta_m$, and also vanishes. For the vortex, the maximum current occurs when $\Delta_i = 1.5L$ and $j_{\parallel, max} = 0.57 \kappa V_0 B_0 L$. For this scale of driver, the current width will be $\Lambda = 2.8 L$ and the width of the electron energy flux, $\Lambda_{\varepsilon} = 2.4L$.

Two important conclusions can be drawn. First, if vortex structures are detected at the ionosphere, they basically map to structures in the boundary layer whereas shear layers only map if the scale is large enough. Second, the current density maximizes when the vortex size maps to the auroral scale length and has roughly the same strength of current density as the shear layer. As vortices become either larger or smaller than the optimal size, the current vanishes. This property suggests that it may be useful to obtain the statistics of spot size versus intensity from auroral images in planetary magnetospheres from which it may be possible to infer ionospheric properties knowing that currents maximize when the width is 1.5L.

Data Availability Statement

References

The DMSP data are available online at a JHU/APL website http://sd-www.jhuapl.edu/Aurora/spectrogram/ index.html. The DMSP SSJ4/SSJ5 and MAG data are also available at NASA CDAWeb https://cdaweb.gsfc. nasa.gov/index.html/, at a Boston College website https://dmsp.bc.edu/, and at a NOAA website https://satdat.ngdc.noaa.gov/dmsp/. DMSP SSUSI data are available at a JHU/APL website https://ssusi.jhuapl.edu/. THEMIS data are available at a UC Berkeley website http://themis.ssl.berkeley.edu/index.shtml.

Auster, H. U., Glassmeier, K. H., Magnes, W., Aydogar, O., Baumjohann, W., Constantinescu, D., et al. (2008). The THEMIS fluxgate magnetometer, Space Science Reviews, 141(1-4), 235-264, https://doi.org/10.1007/s11214-008-9365-9

Bender, C. M., & Orszag, S. A. (1978). Advanced mathematical methods for scientists and engineers, New York, NY: Springer.

Chao, J. K., Wu, D. J., Lin, C.-H., Yang, Y.-H., Wang, X. Y., Kessel, M., et al. (2002). Models for the size and shape of the earth's magnetopause and bow shock. COSPAR Colloquia Series, 17, 127-135. https://doi.org/10.1016/s0964-2749(02)80212-8

De Keyser, J., & Echim, M. (2013). Electric potential differences across auroral generator interfaces. Annales Geophysicae, 31, 251-261. https://doi.org/10.5194/angeo-31-251-2013

Delamere, P. A., Wilson, R. J., Eriksson, S., & Bagenal, F. (2013). Magnetic signatures of Kelvin-Helmholtz vortices on Saturn's magnetopause: Global survey. Journal of Geophysical Research: Space Physics, 118, 393-404. https://doi.org/10.1029/2012JA018197

Echim, M. M., Lamy, H., De Keyser, J., Maggiolo, R., Gunell, H., & Simon Wedlund, C. L. (2019). A method to estimate the physical properties of magnetospheric generators from observations of quiet discrete auroral arcs. Journal of Geophysical Research: Space Physics, 124(12), 10283-10293. https://doi.org/10.1029/2019JA026969

Echim, M. M., Roth, M., & de Keyser, J. (2007). Sheared magnetospheric plasma flows and discrete auroral arcs: A quasi-static coupling model. Annales Geophysicae, 25, 317-330. https://doi.org/10.5194/angeo-25-317-2007

Echim, M. M., Roth, M., & de Keyser, J. (2008). Ionospheric feedback effects on the quasi-stationary coupling between LLBL and postnoon/ evening discrete auroral arcs. Annales Geophysicae, 26, 913-928. https://doi.org/10.5194/angeo-26-913-2008

Acknowledgments

The Air Force Research Laboratory and the World Data Center provided the DMSP SSJ4/SSJ5 and MAG data. Simon Wing acknowledges the support from NASA (Grant nos. NNX15AJ01G, NNX16AQ87G, 80NSSC20K0704, 80NS-SC19K0843, 80NSSC19K0822, 80NSS-C20K1279, and 80NSSC20K0188). Work at Andrews University is supported by NASA (Grant nos. NNX15AJ01G, NNH15AB17I, NNX16AO87G, 80NSSC19K0270, 80NSSC19K0843, 80NSSC18K0835, 80NSSC20K0355, NNX17AI50G, NNX17AI47G, 80HQTR18T0066, 80NSSC18K1578, and 80NSSC20K0704) and NSF (Grant nos. AGS1832207 and AGS1602855), and Andrews University FRG 201119. Work at Lockheed Martin is supported by NASA (Grant nos. NNX15AJ01G and 80NSSC18K1379), Shiva Kavosi acknowledges the support from NASA (Grant no. 80NSSC18K0661).

JOHNSON ET AL. 13 of 15



- Fairfield, D. H., Otto, A., Mukai, T., Kokubun, S., Lepping, R. P., Steinberg, J. T., et al. (2000). Geotail observations of the Kelvin-Helmholtz instability at the equatorial magnetotail boundary for parallel northward fields. *Journal of Geophysical Research*, 105, 21159–21173. https://doi.org/10.1029/1999JA000316
- Grodent, D., Gustin, J., Gérard, J.-C., Radioti, A., Bonfond, B., & Pryor, W. R. (2011). Small-scale structures in Saturn's ultraviolet aurora. Journal of Geophysical Research, 116, 9225. https://doi.org/10.1029/2011JA016818
- Hallinan, T. J., & Davis, T. N. (1970). Small-scale auroral arc distortions. Planetary and Space Science, 18, 1735–1736. https://doi.org/10.1016/0032-0633(70)90007-3
- Hardy, D. A., Schmitt, L. K., Gussenhoven, M. S., Marshall, F. J., Yeh, H., Shumaker, T. L., et al. (1984). Precipitating Electron and Ion detectors (SSJ/4) for the block 5D/Flights 6-10 DMSP Satellites: Calibration and Data Presentation (Rep. AFGL-TR-84-0317, Air Force Geophys). Hanscom AFB, MA: Hanscom Air Force Base Lab.
- Hasegawa, A. (1975). *Plasma instabilities and nonlinear effects*, New York, NY: Springer-Verlag. https://doi.org/10.1007/978-3-642-65980-5 Hasegawa, H. (2012). Structure and dynamics of the magnetopause and its boundary layers. *Monographs on Environment, Earth and Planets*, 1(2), 71–119. https://doi.org/10.5047/meep.2012.00102.0071
- Hasegawa, H., Fujimoto, M., Takagi, K., Saito, Y., Mukai, T., & RèMe, H. (2006). Single-spacecraft detection of rolled-up Kelvin-Helmholtz vortices at the flank magnetopause. *Journal of Geophysical Research*, 111, A09203. https://doi.org/10.1029/2006JA011728
- Hasegawa, H., Retinò, A., Vaivads, A., Khotyaintsev, Y., André, M., Nakamura, T. K. M., et al. (2009). Kelvin-Helmholtz waves at the Earth's magnetopause: Multiscale development and associated reconnection. *Journal of Geophysical Research*, 114, A12207. https://doi.org/10.1029/2009JA014042
- Ieda, A., Oyama, S., Vanhamäki, H., Fujii, R., Nakamizo, A., Amm, O., et al. (2014). Approximate forms of daytime ionospheric conductance. *Journal of Geophysical Research: Space Physics*, 119(12), 10397–10415. https://doi.org/10.1002/2014JA020665
- Johnson, J. R., & Wing, S. (2015). The dependence of the strength and thickness of field-aligned currents on solar wind and ionospheric parameters. *Journal of Geophysical Research: Space Physics*, 120, 3987–4008. https://doi.org/10.1002/2014JA020312
- Johnson, J. R., Wing, S., & Delamere, P. A. (2014). Kelvin Helmholtz instability in planetary magnetospheres. *Space Science Reviews*, 184, 1–31. https://doi.org/10.1007/s11214-014-0085-z
- Kavosi, S., & Raeder, J. (2015). Ubiquity of Kelvin-Helmholtz waves at earth's magnetopause. Nature Communications, 6, 7019. https://doi.org/10.1038/ncomms8019
- Knight, S. (1973). Parallel electric fields. Planet, 21, 741-750
- Lin, D., Wang, C., Li, W., Tang, B., Guo, X., & Peng, Z. (2014). Properties of Kelvin-Helmholtz waves at the magnetopause under northward interplanetary magnetic field: Statistical study. *Journal of Geophysical Research: Space Physics*, 119, 7485–7494. https://doi.org/10.1002/2014ja020379
- Lotko, W., Sonnerup, B. U. O., & Lysak, R. L. (1987). Nonsteady boundary layer flow including ionospheric drag and parallel electric fields. Journal of Geophysical Research, 92, 8635–8648. https://doi.org/10.1029/JA092iA08p08635
- Lui, A. T. Y., Venkatesan, D., & Murphree, J. S. (1989). Auroral bright spots on the dayside oval. Journal of Geophysical Research, 94, 5515–5522. https://doi.org/10.1029/JA094iA05p05515
- Lundin, R., & Evans, D. S. (1985). Boundary layer plasmas as a source for high-latitude, early afternoon, auroral arcs. *Planetary and. Space Science*, 33, 1389–1406. https://doi.org/10.1016/0032-0633(85)90115-1
- Lyons, L. R. (1980). Generation of large-scale regions of auroral currents, electric potentials, and precipitation by the divergence of the convection electric field. *Journal of Geophysical Research*, 85, 17–24. https://doi.org/10.1029/JA085iA01p00017
- Masters, A., Achilleos, N., Kivelson, M. G., Sergis, N., Dougherty, M. K., Thomsen, M. F., et al. (2010). Cassini observations of a Kelvin-Helmholtz vortex in Saturn's outer magnetosphere. *Journal of Geophysical Research*, 115(A7), A07225. https://doi.org/10.1029/2010JA015351
- Masters, A., Mitchell, D., Coates, A., & Dougherty, M. (2011). Saturn's low-latitude boundary layer: 1. Properties and variability. *Journal of Geophysical Research*, 116. A06210.
- McFadden, J. P., Carlson, C. W., Larson, D., Ludlam, M., Abiad, R., Elliott, B., et al. (2008). The THEMIS ESA plasma instrument and inflight calibration. Space Science Reviews, 141(1-4), 277-302. https://doi.org/10.1007/s11214-008-9440-2
- Merkin, V. G., Lyon, J. G., & Claudepierre, S. G. (2013). Kelvin-Helmholtz instability of the magnetospheric boundary in a three-dimensional global MHD simulation during northward IMF conditions. *Journal of Geophysical Research: Space Physics*, 118, 5478–5496. https://doi.org/10.1002/jgra.50520
- Miura, A. (1997). Compressible magnetohydrodynamic Kelvin-Helmholtz instability with vortex pairing in the two-dimensional transverse configuration. *Physics of Plasmas*. 4, 2871–2885. https://doi.org/10.1063/1.872419
- Otto, A., & Fairfield, D. H. (2000). Kelvin-Helmholtz instability at the magnetotail boundary: MHD simulation and comparison with Geotail observations. *Journal of Geophysical Research*, 105, 21175–21190. https://doi.org/10.1029/1999JA000312
- Paxton, L. J., Meng, C.-I., Fountain, G. H., Ogorzalek, B. S., Darlington, E. H., Gary, S. A., et al. (1993). SSUSI: horizon-to-horizon and limb-viewing spectrographic imager for remote sensing of environmental parameters. In R. E. Huffman (Ed.), Proceedings of the Meeting, 20-21 July 1992, Society of Photo-Optical Instrumentation Engineers (SPIE) Conference Series. 1764 (pp. 161–176). San Diego. https://doi.org/10.1117/12.140846
- Potemra, T. A., Erlandson, R. E., Vo, H., Venkatesan, D., & Cogger, L. L. (1990). Periodic auroral forms and geomagnetic field oscillations in the 1400 MLT region. *Journal of Geophysical Research*, 95, 5835–5844. https://doi.org/10.1029/JA095iA05p05835
- Ray, L. C., Galand, M., Delamere, P. A., & Fleshman, B. L. (2013). Current-voltage relation for the Saturnian system. *Journal of Geophysical Research: Space Physics*, 118, 3214–3222. https://doi.org/10.1002/jgra.50330
- Ray, L. C., Su, Y. J., Ergun, R. E., Delamere, P. A., & Bagenal, F. (2009). Current-voltage relation of a centrifugally confined plasma. *Journal of Geophysical Research*, 114(A4), A04214. https://doi.org/10.1029/2008JA013969
- Rich, F. J., Hardy, D. A., & Gussenhoven, M. S. (1985). Enhanced ionosphere-magnetosphere data from the DMSP satellites. *EOS*, 66, 513. Robinson, R. M., & Vondrak, R. R. (1984). Measurements of E region ionization and conductivity produced by solar illumination at high latitudes. *Journal of Geophysical Research*, 89, 3951–3956. https://doi.org/10.1029/JA089iA06p03951
- Robinson, R. M., Vondrak, R. R., Miller, K., Dabbs, T., & Hardy, D. (1987). On calculating ionospheric conductances from the flux and energy of precipitating electrons. *Journal of Geophysical Research*, 92, 2565–2569. https://doi.org/10.1029/JA092iA03p02565
- Shue, J. H., Song, P., Russell, C. T., Steinberg, J. T., Chao, J. K., Zastenker, G., et al. (1998). Magnetopause location under extreme solar wind conditions. *Journal of Geophysical Research*, 103(A8), 17691–17700. https://doi.org/10.1029/98JA01103
- Simon Wedlund, C., Lamy, H., Gustavsson, B., Sergienko, T., & Brändström, U. (2013). Estimating energy spectra of electron precipitation above auroral arcs from ground-based observations with radar and optics. *Journal of Geophysical Research: Space Physics*, 118, 3672–3691. https://doi.org/10.1002/jgra.50347

JOHNSON ET AL. 14 of 15



- Sonnerup, B. U. O. (1980). Theory of the low-latitude boundary layer. Journal of Geophysical Research, 85, 2017–2026. https://doi.org/10.1029/JA085iA05p02017
- Spreiter, J. R., & Stahara, S. S. (1985). Magnetohydrodynamic and gasdynamic theories for planetary bow waves. Washington, DC: American Geophysical Union.
- Talboys, D. L., Arridge, C. S., Bunce, E. J., Coates, A. J., Cowley, S. W. H., & Dougherty, M. K. (2009a). Characterization of auroral current systems in Saturn's magnetosphere: High-latitude Cassini observations. *Journal of Geophysical Research (Space Physics)*, 114, A06220. https://doi.org/10.1029/2008JA013846
- Talboys, D. L., Arridge, C. S., Bunce, E. J., Coates, A. J., Cowley, S. W. H., Dougherty, M. K., & Khurana, K. K. (2009b). Signatures of field-aligned currents in Saturn's nightside magnetosphere. *Geophysical Research Letters*, 36, L19107. https://doi.org/10.1029/2009GL039867
- Talboys, D. L., Bunce, E. J., Cowley, S. W. H., Arridge, C. S., Coates, A. J., & Dougherty, M. K. (2011). Statistical characteristics of field-aligned currents in Saturn's nightside magnetosphere. *Journal of Geophysical Research*, 116, A04213. https://doi.org/10.1029/2010JA016102
- Tsyganenko, N. A., & Stern, D. P. (1996). Modeling the global magnetic field of the large-scale Birkeland current systems. *Journal of Gephysical Research*, 101(27), 187.
- $Wallis, D.\ D., \&\ Budzinski, E.\ E.\ (1981).\ Empirical\ models\ of\ height\ integrated\ conductivities. \textit{Journal of Geophysical Research}, 86 (A1), 125. \\ https://doi.org/10.1029/ja086ia01p00125$
- Wei, C. Q., & Lee, L. C. (1993). Coupling of magnetopause-boundary layer to the polar ionosphere. *Journal of Geophysical Research*, 98, 5707–5725. https://doi.org/10.1029/92JA02232
- Wing, S., & Johnson, J. R. (2015). Theory and observations of upward field-aligned currents at the magnetopause boundary layer. *Geophysical Research Letters*, 42, 9149–9155. https://doi.org/10.1002/2015GL065464
- Zhang, Y., & L. J. Paxton (2008), An empirical Kp-dependent global auroral model based on TIMED/GUVI FUV data, 70, 1231–1242, https://doi.org/10.1016/j.jastp.2008.03.008

JOHNSON ET AL. 15 of 15